RSC Advances

ROYAL SOCIETY OF CHEMISTRY

PAPER

View Article Online
View Journal | View Issue

Cite this: *RSC Adv.*, 2024, **14**, 37697

Chemical synthesis, characterization, and anticancer potential of $CuO/ZrO_2/TiO_2/RGO$ nanocomposites against human breast (MCF-7) cancer cells

ZabnAllah M. Alaizeri, *[a] Hisham A. Alhadlaq, [a] Saad Aldawood[a] and Maqusood Ahamed [b]

Received 30th September 2024
Accepted 13th November 2024

DOI: 10.1039/d4ra07039a

rsc.li/rsc-advances

Nanocomposites (NCs) have attractive potential applications in gas-sensing, energy, photocatalysis, and biomedicine. In the present work, the fabrication of $CuO/ZrO_2/TiO_2/RGO$ nanocomposites (NCs) was done *via* a simple chemical route. Our aim in this work was to synthesis and investigate the selective anticancer activity of TiO_2 NPs by supporting CuO, ZrO_2, and RGO toward cancer and normal cells. Different analytical techniques, such as X-ray diffraction (XRD), high-resolution transmission electron microscopy (HRTEM), scanning electron microscopy (SEM) with energy dispersive X-ray (EDX), X-ray photoelectron spectroscopy (XPS), Raman spectroscopy, Fourier transform infrared (FTIR) spectroscopy, photoluminescence (PL) spectroscopy, and dynamic light scattering (DLS), were carefully applied to characterize the physicochemical properties of the produced samples. XRD results showed that the phase and crystal structure of TiO_2 NPs were enhanced after adding CuO, ZrO_2, and RGO. TEM and SEM images showed that $CuO/ZrO_2/TiO_2/RGO$ NCs were similarly distributed on RGO sheets with high crystallinity, excellent quality of lattice fringes, and lower agglomeration compared with pure TiO_2 NPs. EDX and XPS analysis confirmed the presence of elements Cu, Zr, Ti, O, and C in the obtained $CuO/ZrO_2/TiO_2/RGO$ NCs. Raman and FTIR spectra verified the presence of functional groups and crystal structures in the produced samples. PL data showed that the optical properties of TiO_2 improved after adding CuO, ZrO_2, and RGO sheets owing to the reduction in the recombination rate between the electron–hole pair. DLS analysis showed that the prepared $CuO/ZrO_2/TiO_2/RGO$ NCs had excellent colloidal stability and good distribution in the suspension of the media culture. Anticancer results for $CuO/ZrO_2/TiO_2/RGO$ NCs exhibited about 2-fold higher toxicity for 24 h and 4-fold for 48 h against breast cancer (MCF-7) cells than pure TiO_2 NPs, while their biocompatibility was excellent against HUVEC normal cells. Additionally, the IC_{50} values of $CuO/ZrO_2/TiO_2/RGO$ NCs were $44.19 \pm 1.2\ \mu g\ mL^{-1}$ and $24.52 \pm 0.8\ \mu g\ mL^{-1}$ for 24 h and 48 h, respectively. These results indicate that adding CuO, ZrO_2, and RGO plays a crucial role in enhancing the anticancer property of TiO_2 NPs. This study suggests that $CuO/ZrO_2/TiO_2/RGO$ NCs could be applied in cancer therapy applications in *in vivo* models.

1. Introduction

Due to their tailorable drug delivery, enhanced bioavailability, and low toxicity, nanomaterials have potential medical applications, including in cancer therapy and diagnostics.[1,2] The high development cost, toxicity concerns, and targeting accuracy of some nanomaterials pose challenges in their application in medicine.[3] To resolve these obstacles, common nanomaterials have excellent properties, such as low toxicity and high biocompatibility.[4] Currently, titanium dioxide nanoparticles (TiO_2 NPs) are important in potential applications in environmental remediation and medical fields owing to their excellent physicochemical properties.[5,6] Despite these advantages, pure TiO_2 NPs exhibit some limitations in cancer therapy.[7] One major limitation of TiO_2 NPs is their agglomeration due to their high surface energy, which reduces their colloidal stability and hampers their bioavailability in cellular environments.[8] Previous studies have shown that the integration of other metal oxides, such as CeO_2 NPs,[9] SnO_2 NPs,[10] ZnO NPs,[11] CuO NPs,[12] ZrO_2 NPs,[13] Al_2O_3 NPs,[14] and WO_3 NPs,[15] can improve their anticancer properties. Generally, nanocomposites (NPs) are a type of nanomaterials that are produced by the combination of two or multi-metal oxides to enhance their

---

[a] Department of Physics and Astronomy, College of Science, King Saud University, Riyadh 11451, Saudi Arabia. E-mail: zabn1434@gmail.com

[b] King Abdullah Institute for Nanotechnology, King Saud University, Riyadh 11451, Saudi Arabia

physicochemical properties for potential applications in photocatalytic and medical fields.[16,17]

To enhance the properties of metal oxide NPs, many researchers have focused on improving different approaches (chemical, physical, and biological) to synthesize novel nanocomposites (NCs), which are mixed with metal oxide NCs. Particularly, chemical approaches such as hydrothermal, sol–gel, co-precipitation, and thermal decomposition techniques have been applied to the synthesis of NCs due to their low cost and environmental friendliness.[18–20] For example, Kubiak *et al.*[21] prepared ZnO/TiO_2, ZrO_2/TiO_2 and MoS_2/TiO_2 NCs using the hydrothermal method with enhanced antibacterial and photocatalytic activities compared to pure TiO_2 NPs. Another study[22] reported that the sol–gel method was used to synthesize SnO_2/WO_3 NCs with highly improved optical properties compared with WO_3 NPs. Moreover, CuO/NiO/ZnO NCs have been synthesized *via* the co-precipitation process, and they show highly enhanced antibacterial activity compared to individual samples.[23] Correspondingly, Marsooli *et al.*[24] synthesized $Fe_2O_4/CdWO_4/PrVO_2$ NCs through the precipitation method, which exhibits excellent anticancer performance. Indumathi *et al.*[25] prepared CuO/TiO_2/chitosan-farnesol NCs by standard acetic acid synthesis to investigate antimicrobial and anticancer activities toward melanoma cancer cells.

Reduced graphene oxide (RGO) has attracted potential biomedical applications such as cancer therapy owing to its excellent characteristics.[26] Numerous studies show that different metal oxide NPs combined with RGO can improve their synthesis and anticancer properties. For instance, Ahamed and Kadiyala *et al.*[27,28] reported that ZrO_2/RGO NCs have enhanced cytotoxicity against cancer cells while maintaining biocompatibility with normal cells. Similarly, Scotti *et al.*[29] showed that ZnO/ZrO_2/RGO NCs exhibit 3.5-fold higher anticancer efficacy against lung and breast cancer cells compared to ZnO NPs. Besides, our previous study[30] investigated that Bi_2O_3-doped WO_3/RGO NCs have enhanced anticancer activity and better biocompatibility than both NPs. The synthesized ZnO–TiO_2/RGO NCs showed improved cytotoxicity towards cancer cells and better biocompatibility compared to normal cells.[31,32] Askari *et al.*,[33] investigated that Mn_2O_4/Co_3O_4/RGO NCs have a good ability to inhibit the growth of cancer cells.

The purpose of this work was to fabricate $CuO/ZrO_2/TiO_2$/RGO NCs to enhance the selective anticancer activity toward human cancer and normal cell lines. The prepared samples were further characterized by XRD, HRTEM, and SEM with EDX, XPS, Raman, FTIR, PL, and DLS techniques to envisage the enhanced physicochemical properties. In the present work, MTT assay was applied to assess the selective anticancer performance of the prepared samples against breast cancer cells and HUVEC normal cells for 24 h and 48 h.

2. Experimental

2.1 Chemicals and cells

Titanium butoxide Ti $(OBu)_4$, zirconium nitrate pentahydrate $(Zr(NO_3)_4\cdot 5H_2O)$, $Cu(NO_3)_2\cdot 6H_2O$, and sodium hydroxide (NaOH) were supplied by Sigma-Aldrich in St. Louis, MO, USA. Dulbecco's Modified Eagle Medium (DMEM), fetal bovine serum (FBS), MTT (3-(4,5-dimethylthiazol-2-yl)-2,5-diphenyltetrazolium bromide), and dimethyl sulfoxide (DMSO) were also obtained from Sigma-Aldrich in St. Louis, MO, USA. Human breast (MCF-7) cancer and Human Umbilical Vein Endothelial Cells (HUVEC) cells were bought from the American Type Culture Collection (ATTC) based in Manassas, WV, USA.

2.2 Preparation of $CuO/ZrO_2/TiO_2$ nanocomposites (NCs)

The preparation of $CuO/ZrO_2/TiO_2$ NCs (0.5 : 0.5 : 1 mol ratio) was achieved using a co-precipitation process. Firstly, 0.01 mol of $Ti(OBu)_4$ was slowly added to 50 mL of absolute ethanol under stirring. Then, 0.005 mol of $Zr(NO_3)_4\cdot 5H_2O$ and 0.0025 mol of $Cu(NO_3)_2\cdot 6H_2O$ were further added into the above solution under stirring for 1 h at room temperature. Next, 1 M of NaOH was dropped slowly to the mixture solution with stirring at 65 °C for 4 h to obtain the precipitate. Subsequently, the obtained precipitate was filtered, washed with ethanol and water several times, and dried in an oven at 80 °C for 12 h. The calcination for the dried precipitate was carried out using an oven at 500 °C under air for 5 h to obtain $CuO/ZrO_2/TiO_2$ NCs as a nanopowder. Under the same protocols, pure TiO_2 NPs were successfully prepared without using $Zr(NO_3)_4\cdot 5H_2O$ and $Cu(NO_3)_2\cdot 6H_2O$. Similarly, ZrO_2/TiO_2 NCs were synthesized without using $Zr(NO_3)_4\cdot 5H_2O$.

2.3 Preparation of $CuO/ZrO_2/TiO_2$/RGO nanocomposites (NCs)

The $CuO/ZrO_2/TiO_2$ NCs were successfully anchored onto RGO sheets *via* the sonication process. A specific amount of $CuO/TiO_2/ZrO_3$ NCs was suspended in 50 mL ethanol and distilled water (1 : 1) under ultrasonication for 1 h as the first solution. 10% of reduced graphene oxide (RGO) sheets were dissolved in 50 mL ethanol under stirring for 1 h as the second solution. Then, the two solutions were mixed and sonicated for 4 h at 80 kW. Next, the mixture solution was further dried at 60 °C for 24 h to obtain $CuO/ZrO_2/TiO_2$/RGO NCs.

2.4 Characterization methods

Different analytical techniques, such as XRD, HRTEM, SEM with EDX, XPS, Raman, FTIR, PL, and DLS, effectively characterized the physicochemical properties of the obtained NPs and NCs. Thus, the details of these techniques are mentioned in our previous works.[34,35]

2.5 Cell culture and maintenance

Human breast (MCF-7) cancer and HUVEC normal cells were cultured in DMEM supplemented with 10% fetal bovine serum (FBS), 1% penicillin–streptomycin, and 1% glutamine in the flask. The cultured cells were maintained at 37 °C in a humidified atmosphere with 5% CO_2. Further details were done in our published studies.[36,37]

2.6 Anticancer and biocompatibility performance

In the present work, the evaluation of the anticancer activity of the prepared samples was estimated using the MTT assay as reported in our pervious study.[34] Briefly, about 5 × 10^4 cells per well were seeded in a 96-well plate and incubated at 37 °C with 5% CO_2. Then, the stock solution (3 mg/3 mL) of the prepared samples in DMEM was successfully prepared. A section of each sample was also diluted to different concentrations (0, 0.5, 1, 5, 10, 25, 50, and 100 μg mL^{-1}). The next day, these different concentrations of each sample were added to the seeded cells in a 96-well plate with incubation at 37 °C with 5% CO_2 for 24 h and 48 h. After the incubation period, the DMEM of each well without the control was removed. Then, 20 μL of MTT solution (5 mg mL^{-1}) was added to each well and incubated for 4 h. Following this, 100 μL of DMSO formazan crystals formed by metabolically active cells were dissolved. The absorbance was measured at 570 nm using a microplate reader. The cell viability was calculated as a percentage relative to the untreated control cells, and the IC_{50} values (the concentration at which 50% of the cells are inhibited) were determined.

2.7 Data analysis

Data analysis in all experiments was done using one-way analysis of variance (ANOVA) as mean ± standard deviation. A *p*-value of <0.05 was considered statistically significant.

3. Results and discussion

3.1 XRD study

X-ray diffraction (XRD) analysis of the synthesized NPs and NCs was done to determine their phase and crystallinity. Fig. 1a–d illustrates the XRD spectra of the obtained pure TiO_2 NPs, ZrO_2/TiO_2 NCs, $CuO/ZrO_2/TiO_2$ NCs, and $CuO/ZrO_2/TiO_2$/RGO NCs. The XRD spectra of pure TiO_2 NPs (Fig. 1a) observed that the diffraction peaks were associated to 2θ values of 25.3°, 37.8°,48.0°, 55.1°, 62.9°, 70.0°, and 75.3° corresponding to the (101), (004), (200), (211), (204), (220), and (215) planes, respectively.[38] These spectra reveal that pure TiO_2 NPs have high crystallinity and purity without the presence of impurities. Hence, Fig. 1b exhibits new peaks at 30.3° and 50.4°, corresponding to the crystalline and phase of ZrO_2, as reported in a preceding investigation.[39] This indicates that the ZrO_2/TiO_2 NCs were successfully prepared with a change in their crystallinity. For $CuO/ZrO_2/TiO_2$ NCs (Fig. 1c), the XRD spectra display all peaks corresponding to CuO, ZrO_2, and TiO_2. Furthermore, the peaks at 35.5° and 38.7° confirmed the presence of the monoclinic phase of CuO in the synthesized $CuO/ZrO_2/TiO_2$ NCs.[40] This phenomena reveals that there is a change in the crystal structure of ZrO_2/TiO_2 NCs after adding CuO. In addition, the XRD spectra of $CuO/ZrO_2/TiO_2$/RGO NCs (Fig. 1d) exhibit the peaks for all three metal oxides (CuO, ZrO_2, and TiO_2) along with a broad peak at 24°, signifying the amorphous nature of reduced graphene oxide (RGO). By the Scherrer equation,[41] the average crystallite sizes of pure TiO_2 NPs, ZrO_2/TiO_2 NPs, $Cu/ZrO_2/TiO_2$ NCs, and $CuO/ZrO_2/TiO_2$/RGO NCs were 10.1 ± 1.2 nm, 16.0 ± 1.5 nm, 50.3 ± 0.9 nm, and 52.1 ± 0.6 nm, respectively. XRD results showed that the supporting ZrO_2, CuO, and RGO strongly contributed to improving the structural properties of TiO_2, such as their crystallinity, phase purity, and increased crystallite size. This study highlighted that $CuO/ZrO_2/TiO_2$/RGO NCs could progress their performance in potential applications. Several earlier studies[42–45] were matched with the obtained XRD results.

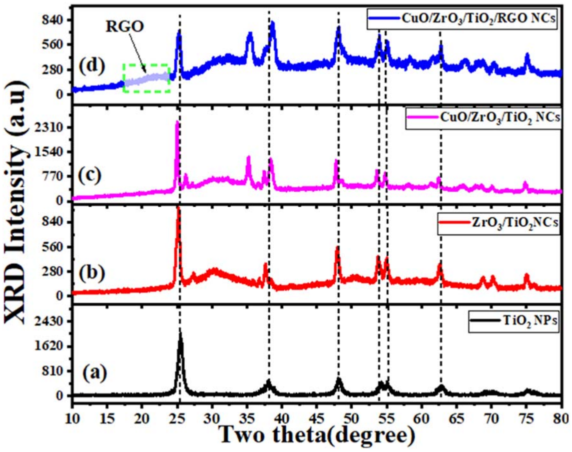

Fig. 1 XRD pattern: (a) pure TiO_2 NPs, (b) ZrO_2/TiO_2 NPs, (c) $CuO/ZrO_2/TiO_2$ NCs, and (d) $CuO/ZrO_2/TiO_2$/RGO NCs.

3.2 TEM study

Fig. 2A–I depicts the TEM, HRTEM images and SAED analysis of the produced pure TiO_2 NPs, $CuO/ZrO_2/TiO_2$ NCs, and $CuO/ZrO_2/TiO_2$/RGO NCs. The TEM image of pure TiO_2 NPs (Fig. 2A) displays that their morphology was spherical and uniformly distributed with high agglomeration, and the average particle size was 9.2 ± 1.9 nm, as reported in a recent study.[46] Moreover, the HRTEM image (Fig. 2B) verifies the crystal structure of pure TiO_2 NPs by calculating the *d*-spacing value of 0.365 nm, which matches the (101) planes.[47] Likewise, the SAED pattern (Fig. 2C) exhibits distinct diffraction rings, further confirming the crystallinity of TiO_2 in the anatase phase, which corresponds to the (101), (004), (200), and (211) planes. After the incorporation of CuO and ZrO_2, as shown in Fig. 3D, the produced TiO_2 NPs demonstrate a more heterogeneous morphology with the lowest agglomeration and particle size of about 46.9 ± 1.3 nm. The HRTEM image (Fig. 2E) reveals that the *d*-spacing values of TiO_2 NPs, ZrO_2, and CuO in $CuO/ZrO_2/TiO_2$ NCs were 0.337 nm, 0.266 nm, and 0.271 nm, corresponding to the (101), (111), and (002) planes, respectively, as matched with a previous study.[48] Also, the SAED pattern (Fig. 2F) exhibits additional diffraction rings compared to that of pure TiO_2(101), corresponding to CuO(111) and ZrO_2(002). These phenomena indicate that the addition of CuO and ZrO_2 could change the crystal structure of TiO_2 NPs. Additionally, TEM images (Fig. 2G) confirmed that the synthesized $CuO/ZrO_2/TiO_2$ NCs were anchored onto RGO sheets with a slight reduction in the agglomeration compared to both pure TiO_2 NPs and $CuO/ZrO_2/TiO_2$ NCs, as reported in some recent investigations. The average size of the particles was approximately 53.1 nm. However, the *d*-spacing for TiO_2, ZrO_2, and CuO was found be 0.277 nm, 0.29 nm, and 0.156 nm, respectively, as revealed in Fig. 2H. These values confirm the

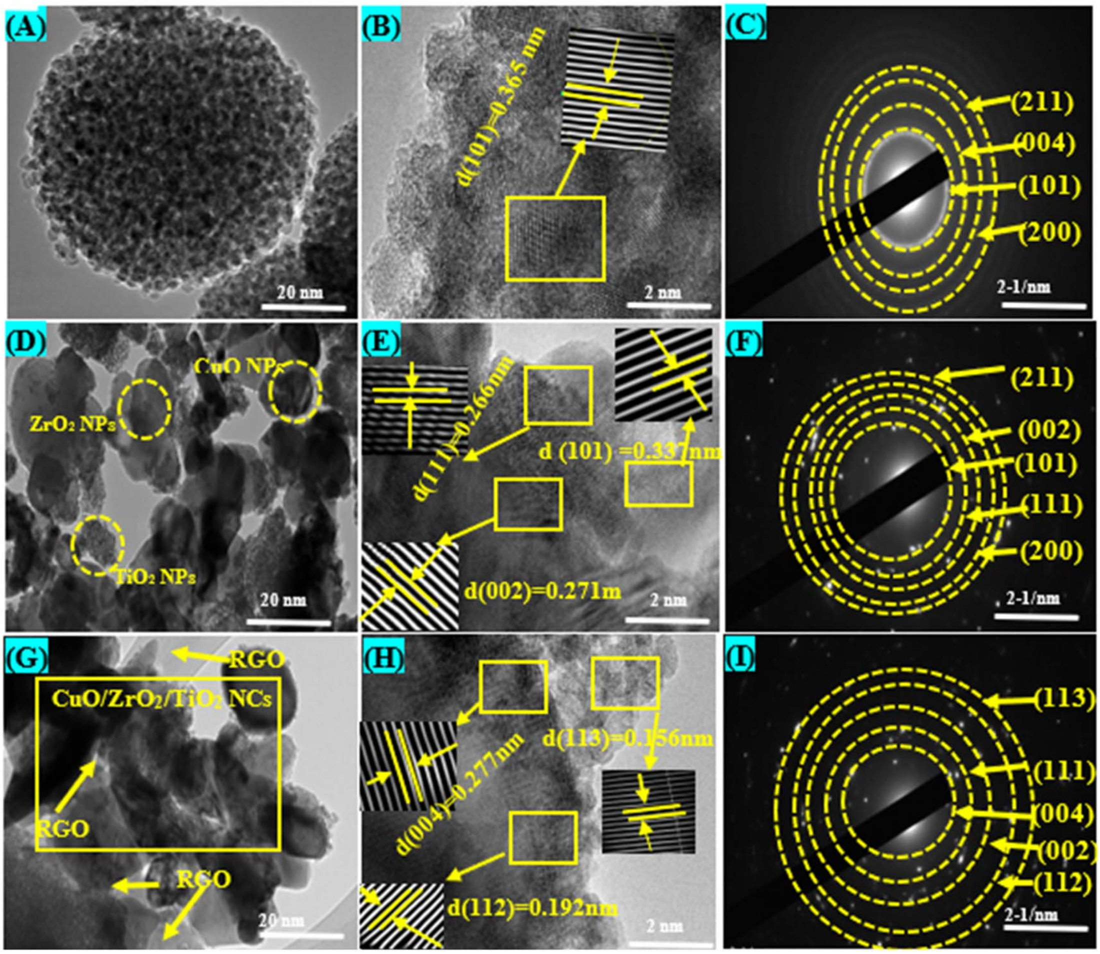

Fig. 2 TEM and HR-TEM images with SAED analysis: (A–C) pure TiO_2 NPs, (D–F) $CuO/ZrO_2/TiO_2$ NCs, and (G–I) $CuO/ZrO_2/TiO_2/RGO$ NCs.

presence of all three components in the prepared $CuO/ZrO_2/TiO_2/RGO$ NCs. The SAED pattern (Fig. 2I) shows distinct spots and rings indicative of a polycrystalline structure, confirming the presence of RGO and further supporting the homogeneity of the NCs. These TEM images suggest that supporting RGO on $CuO/ZrO_2/TiO_2$ NCs enhances the photocatalytic and anticancer performance. Similar studies[49–52] were supported by the presented TEM results.

3.3 SEM and EDX with elemental mapping analysis

SEM analysis was achieved to investigate the morphologies of the prepared samples, as displayed in Fig. 3A–D. Pure TiO_2 NPs (Fig. 3A) show an agglomerated morphology with densely packed spherical particles, in agreement with an earlier report.[53] Consistently, ZrO_2/TiO_2 NCs (Fig. 3B) exhibit a more compact structure with more uniform distributions and increased particle aggregation. We observed that the addition of ZrO_2 played a role in changing of the surface morphology and the particle sizes compared to the TEM image of pure TiO_2 NPs, in agreement with an earlier study.[54] This phenomenon confirms the successful reaction between ZrO_2 and TiO_2 NCs to produce ZrO_2/TiO_2 NCs. The prepared $CuO/ZrO_2/TiO_2$ NCs (Fig. 3C) show a rougher and more uniformly distributed surface, indicating enhanced particle interaction due to CuO inclusion.[55] Fig. 3D confirms that the prepared $CuO/ZrO_2/TiO_2$ NPs were adhered onto RGO sheets, as reported in a previous study.[56] These results suggest that $CuO/ZrO_2/TiO_2/RGO$ NCs reveal well-dispersed NCs supported on RGO sheets, preventing aggregation and maximizing the effective surface area for biological applications.

The EDX and elemental mapping analysis of the synthesized $CuO/ZrO_2/TiO_2/RGO$ NCs are presented in Fig. 4A–J. Hence, the EDX spectra (Fig. 4A) verified that the elemental compositions of the prepared sample are in agreement with their percentage in the synthesis process. Fig. 4B displays the electron image of the sample, which displays the surface morphology and distribution of NCs. The elemental mapping analysis (Fig. 4C–J) confirmed that the elements (Cu, Zr, Ti, O, and C) were present with highly uniform distribution in the obtained $CuO/ZrO_2/TiO_2/RGO$ NCs. As shown in these results, the anchoring of $CuO/ZrO_2/TiO_2$ NCs onto the RGO sheet plays a role in enhancing their surface morphologies and structure for potential applications such as environmental remediation and therapy. These results are in excellent agreement with a previous study.[57–59]

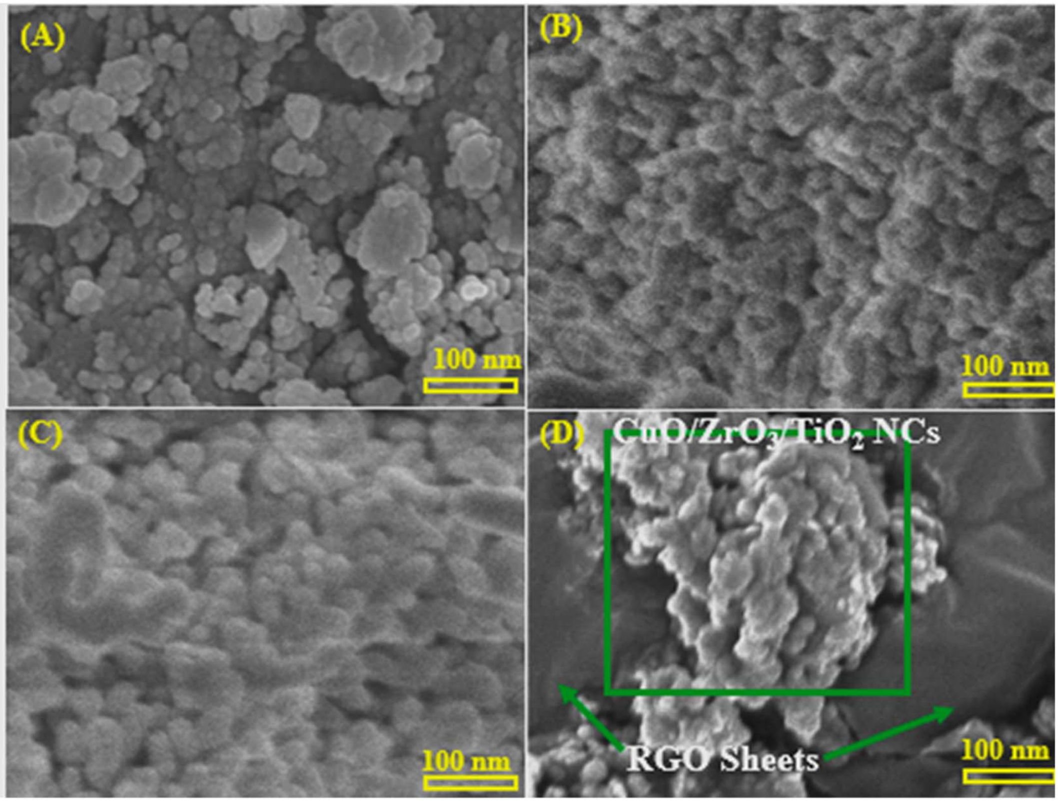

Fig. 3 Scanning electron microscopy (SEM) images: (A) pure TiO_2 NPs, (B) ZrO_2/TiO_2 NCs, (C) $CuO/ZrO_2/TiO_2$ NCs, and (D) $CuO/ZrO_2/TiO_2/RGO$ NCs.

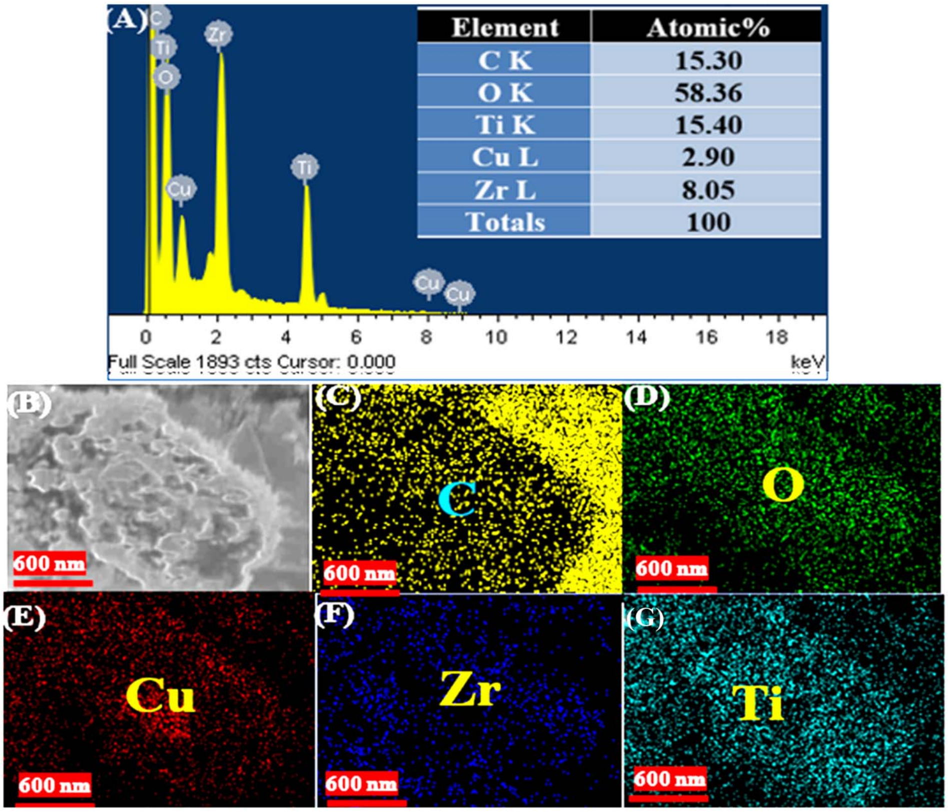

Element	Atomic%
C K	15.30
O K	58.36
Ti K	15.40
Cu L	2.90
Zr L	8.05
Totals	100

Fig. 4 EDX with elemental mapping of the synthesized $CuO/ZrO_2/TiO_2/RGO$ NCs: (A) EDX spectra, (B) electron image, (C) carbon (C), (D) oxygen (O), (E) copper (Cu), (F) zirconium (Zr), and (G) titanium (Ti).

3.4 XPS analysis

The evaluation of the chemical composition and the oxidation states of all elements in the prepared samples were further analyzed by XPS technique. Fig. 5A–F depicts the XPS spectra of the survey and the high-resolution spectra of Cu 2p, Zr 3d, Ti 2p, O 1s, and C 1s. Thus, the XPS spectra (Fig. 5A) of the survey exhibited the presence of all elements Cu, Zr, Ti, O, and C in the produced CuO/ZrO_2/TiO_2/RGO NCs with high purity, consistent with similar studies.[60,61] In Fig. 5B, the high-resolution spectra of Cu CuO/ZrO_2/TiO_2/RGO NCs 2p (Fig. 5B) reveals two characteristic peaks at binding energies (B.E) of 935.5 eV and 955.8 eV corresponding to Cu $2p_{3/2}$ and Cu $2p_{1/2}$, respectively, in agreement with earlier studies.[62,63] These peaks are related to the presence of Cu^{2+} in CuO, as shown through the energy difference of ∼20.3 eV between the two peaks. Also, the 940–949 eV range of B.E represents satellite peaks, which confirm the existence of Cu^{2+} species. From the XPS spectra of Zr 3d (Fig. 5C), the B.E of Zr $3d_{5/2}$ and Zr $3d_{3/2}$ was located at 183.3 eV and 185.7 eV, respectively. It can be shown that the Zr 3d doublet splitting of roughly 2.4 eV verifies the stability of Zr in its oxidation state.[64] The XPS spectra of Ti 2p (Fig. 5D) displays two peaks, which are located at 459.6 eV and 465 eV, respectively. These peaks indicate that the oxidized Ti^{4+} species was present in TiO_2 within the CuO/ZrO_2/TiO_2/RGO NCs.[65] Furthermore, three distinct XPS peaks of O 1s were further assigned at 529.8 eV, 531.3 eV, and 532.5 eV, respectively. Besides, the peak at 529.8 eV is produced due to the lattice oxygen in the structure of CuO, ZrO_2, and TiO_2 NPs. The peaks at 531.3 eV and 532.5 eV were attributed to oxygen defect or hydroxyl group and chemisorbed water on the surface of the prepared NCs, respectively.[66] On the other hand, the three main peaks at B.E of 283.8 eV, 285.3 eV, and 289.5 eV corresponded to the XPS spectra of C 1s (Fig. 5F). It can be observed that the sp^2-hybridized carbon atoms (C=C) present in the RGO framework are assigned at 283.8 eV. The peaks at 285.2 eV and 289.5 eV are due to C–C and C–O bonds, respectively.[67] Our XPS results indicate that the addition of CuO, ZrO_2, and TiO_2 NPs into RGO sheets exhibited distinct binding energies corresponding to the Cu^{2+}, Zr^{4+}, Ti^{4+}, and O^{2-} species in the presence of sp^2-hybridized carbon in RGO. These binding energies of elements have a contribution in the enhanced catalytic or electronic properties of these NCs.

3.5 Raman analysis

The Raman spectra (Fig. 6A and B) display vibrational modes of the produced pure TiO_2 NPs, ZrO_2/TiO_2 NCs, CuO/ZrO_2/TiO_2 NCs, and CuO/ZrO_2/TiO_2/RGO NCs. The Raman band of pure TiO_2 (Fig. 6A(I)) were exhibited at 148.7 cm^{-1}, 403.2 cm^{-1}, 520.1 cm^{-1}, and 644.8 cm^{-1} with high intensity.[68] For ZrO_2/TiO_2 NCs (Fig. 6A(II)), the shift of the Raman bands at 146.1 cm^{-1}, 400.6 cm^{-1}, 520.1 cm^{-1}, and 639.6 cm^{-1}, respectively, was observed as agreed with previous studies.[69,70] We observed that the Raman bands shift to a lower wavenumber. This shift indicates a change in the crystal structure of pure TiO_2 NPs due to the addition of ZrO_2. Upon the addition of CuO in Fig. 6A(III), new peaks appear at about 213 cm^{-1}, characteristic of the CuO phase in a similar study.[71] These results confirmed the successful integration of CuO into the ZrO_2/TiO_2 NCs. As shown in the above results, supporting TiO_2 with CuO or ZrO_2 can introduce defects and surface oxygen vacancies, causing shifts in the Raman peak positions. Fig. 6A and B(IV) display that the introduction of the RGO sheet modifies the Raman bands

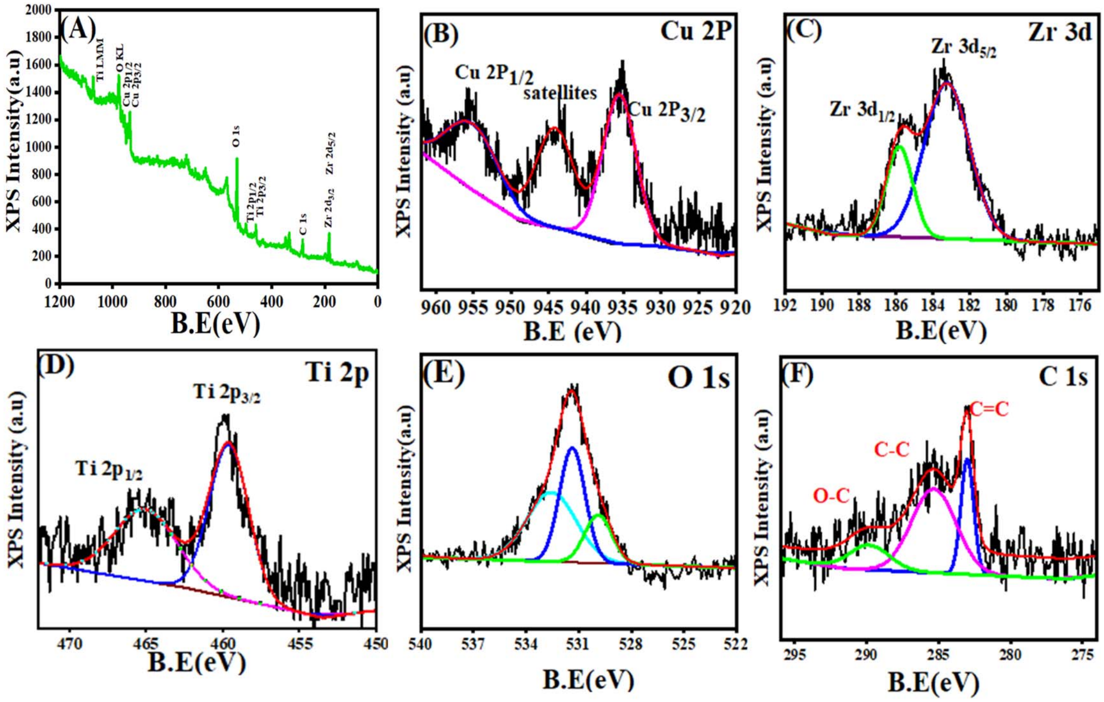

Fig. 5 XPS spectra of CuO/ZrO_2/TiO_2/RGO NCs: (A) survey spectra, (B) Cu 2p, (C) Zr 3d, (D) Ti 2p, (E) O 1s, and (F) C 1s.

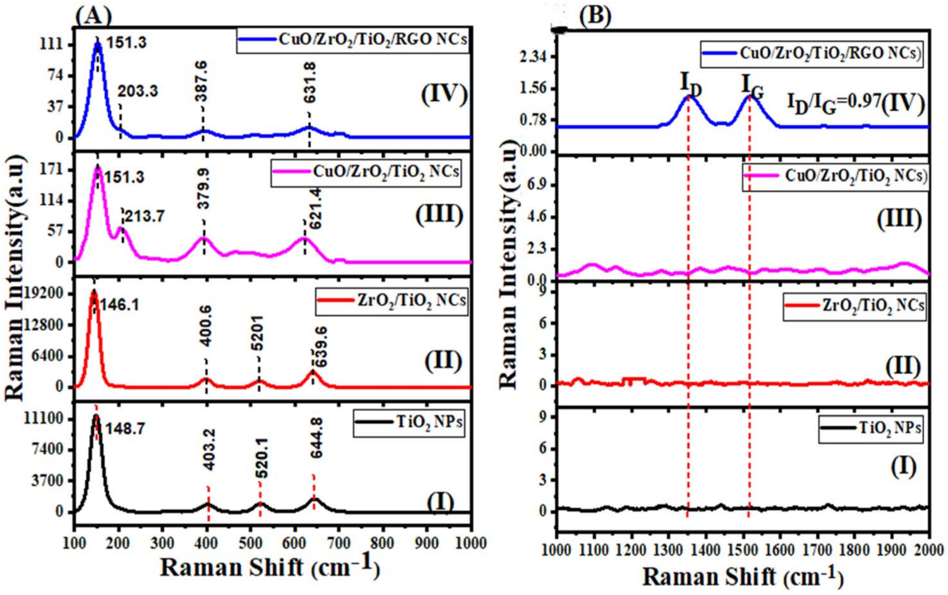

Fig. 6 Raman spectra of pure TiO_2 NPs, ZrO_2/TiO_2 NCs, $CuO/ZrO_2/TiO_2$ NCs, and $CuO/ZrO_2/TiO_2/RGO$ NCs.

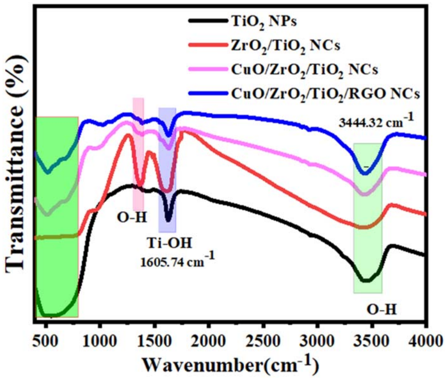

Fig. 7 FT-IR spectra of pure TiO_2 NPs, ZrO_2/TiO_2 NCs, $CuO/ZrO_2/TiO_2$ NCs, and $CuO/ZrO_2/TiO_2/RGO$ NCs.

compared to that of pure TiO_2. Furthermore, Fig. 6B(IV) shows the ratio ($I_D/I_G = 0.97$) between the Raman bands of the RGO sheet.[72] In addition, a decrease in the intensity of the $CuO/ZrO_2/TiO_2/RGO$ NCs peaks is observed, which may be attributed to the interaction between the CuO, ZrO_2, and TiO_2/RGO matrix and RGO. Raman results illustrate that introducing CuO, ZrO_2, and RGO sheets enhanced the crystal structure properties of TiO_2. It suggests that $CuO/ZrO_2/TiO_2/RGO$ NCs are suitable for potential applications such as catalysis and medical and environmental remediation. The XRD and FTIR results (Fig. 1 and 7) were also in good agreement with the Raman results.

3.6 FTIR analysis

The composition and structure of NPs and NCs were further determined through Fourier transform infrared (FT-IR) spectroscopy. Fig. 7 illustrates the FTIR spectra of the synthesized TiO_2 NPs, ZrO_2/TiO_2 NCs, $CuO/ZrO_2/TiO_2$ NCs, and $CuO/ZrO_2/TiO_2/RGO$ NCs. The FTIR spectra demonstrate important absorption bands between 400 and 800 cm^{-1}, which could be attributable to the stretching vibration of Ti–O, Zr–O, and Cu–O.[73,74] Furthermore, the Ti–OH stretching vibrations in all the samples appeared at 1605.74 cm^{-1}. This indicates hydrated molecules due to the hydroxyl group band, as shown in a previous study.[75] We observed that the O–H stretching band of all the samples was assigned at 344.32 cm^{-1}, signifying the successful reduction of graphene oxide and the existence of hydroxyl groups. Significantly, the shifts and intensity changes in the characteristic bands reflect strong interactions between the components, which can improve the physicochemical properties of $CuO/ZrO_2/TiO_2/RGO$ NCs. This indicates the effect on the crystal structure of TiO_2 NCs after the addition of CuO, ZrO_2, and TiO_2, as supported by the XRD and TEM results (Fig. 1 and 2). FTIR results showed that the presence of surface hydroxyls and metal–oxygen bonds highlight the potential of these materials for improved catalytic and anticancer performance.

3.7 Photoluminescence (PL) analysis

The charge recombination behavior of the prepared samples (Fig. 8) was investigated by PL analysis at an excitation wavelength of 325 nm. It can be observed that the PL spectra of pure TiO_2 NPs displays a strong emission peak at about 360–480 nm, corresponding to the near-band-edge emission of the anatase phase of TiO_2. The emission peaks of all the samples appeared at 372.3 nm, 416.5 nm, and 461.1 nm. Upon the incorporation of ZrO_2, it can be observed that the PL intensity of pure TiO_2 NPs was reduced. This reduction indicates improved charge separation due to the formation of heterojunctions between ZrO_2 and TiO_2, which suppresses recombination.[76,77] With the addition of CuO, the PL intensity of pure TiO_2 NPs is further reduced due to the effective charge transfer between CuO and the ZrO_2/TiO_2 NCs, as reported in a previous study.[78] Furthermore, incorporating reduced graphene oxide (RGO) into $CuO/ZrO_2/$

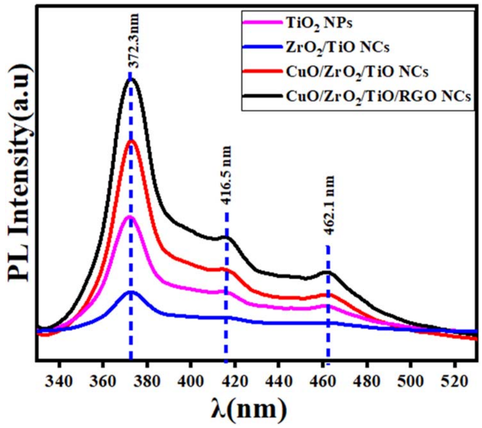

Fig. 8 PL spectra of pure TiO_2 NPs, ZrO_2/TiO_2 NCs, $CuO/ZrO_2/TiO_2$ NCs, and $CuO/ZrO_2/TiO_2/RGO$ NCs.

TiO_2 NCs improves the PL intensity by creating oxygen vacancies and defects, in agreement with some investigations.[79,80] The PL results emphasized that the prepared $CuO/ZrO_2/TiO_2/RGO$ NCs have potential applications, including environmental remediation and therapy.

Table 1 Zeta potential of the prepared samples in the culture media

Sample	Zeta potential (mV ± SD)
TiO_2 NPs	−30.1 ± 4.56
ZrO_2/TiO_2 NCs	−33.9 ± 6.82
$CuO/ZrO_2/TiO_2$ NCs	−34.8 ± 6.77
$CuO/ZrO_2/TiO_2/RGO$ NCs	−35.6 ± 6.92

3.8 Dynamic light scattering (DLS) analysis

The behaviour of the prepared samples and their stability in the culture media were assessed by measuring the particle size distribution and zeta potential, as illustrated in Fig. 9A–D. However, the distribution of particle size of pure TiO_2 NPs, ZrO_2/TiO_2 NPs, $CuO/ZrO_2/TiO_2$ NCs, and $CuO/ZrO_2/TiO_2/RGO$ NC was found to be 365.8 ± 122.6 nm, 320.8 ± 101.0 nm, 256.9 ± 4936 nm, and 250.8 ± 43.7 nm, respectively.[81,82] These values indicate that the distribution of $CuO–ZrO_2–TiO_2/RGO$ NCs was better than each of the prepared sample due to its excellent polydispersity index (PDI = 0.036), while the particles of pure TiO_2 NPs showed high agglomeration, as supported by the TEM results (Fig. 3A, D, and G). The zeta potential values of the prepared samples to evaluate the behaviour of these samples and their stability in the culture media are shown in Table 1. Nevertheless, the zeta potential values of pure TiO_2 NPs, ZrO_2/TiO_2 NPs, $CuO/ZrO_2/TiO_2$ NCs, and $CuO/ZrO_2/TiO_2/RGO$ NC were −30.1 ± 4.56 mV, −33.9 ± 6.82 mV, −34.8 ± 6.77 mV, and −35.6 ± 6.92 mV, as matched with similar studies.[83,84] These values demonstrate that the colloidal stability and distribution of $CuO/ZrO_2/TiO_2/RGO$ NC were greater than those of individual samples in the suspension of the media culture. On the other hand, the negative charges on the surface of NPs and NCs could

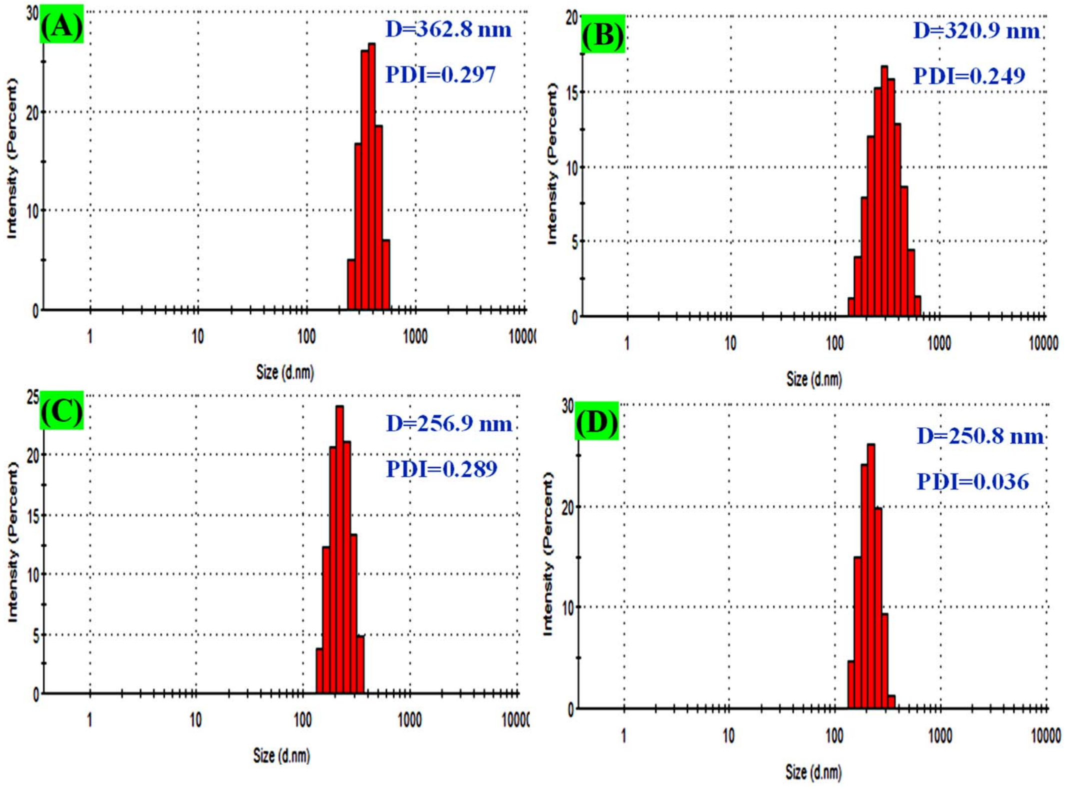

Fig. 9 DLS analysis for particle size distribution: (A) pure TiO_2 NPs, (B) $ZrO_2–TiO_2$ NCs, (C) $CuO–ZrO_2–TiO_2$ NCs, and (D) $CuO–ZrO_2–TiO_2/RGO$ NCs.

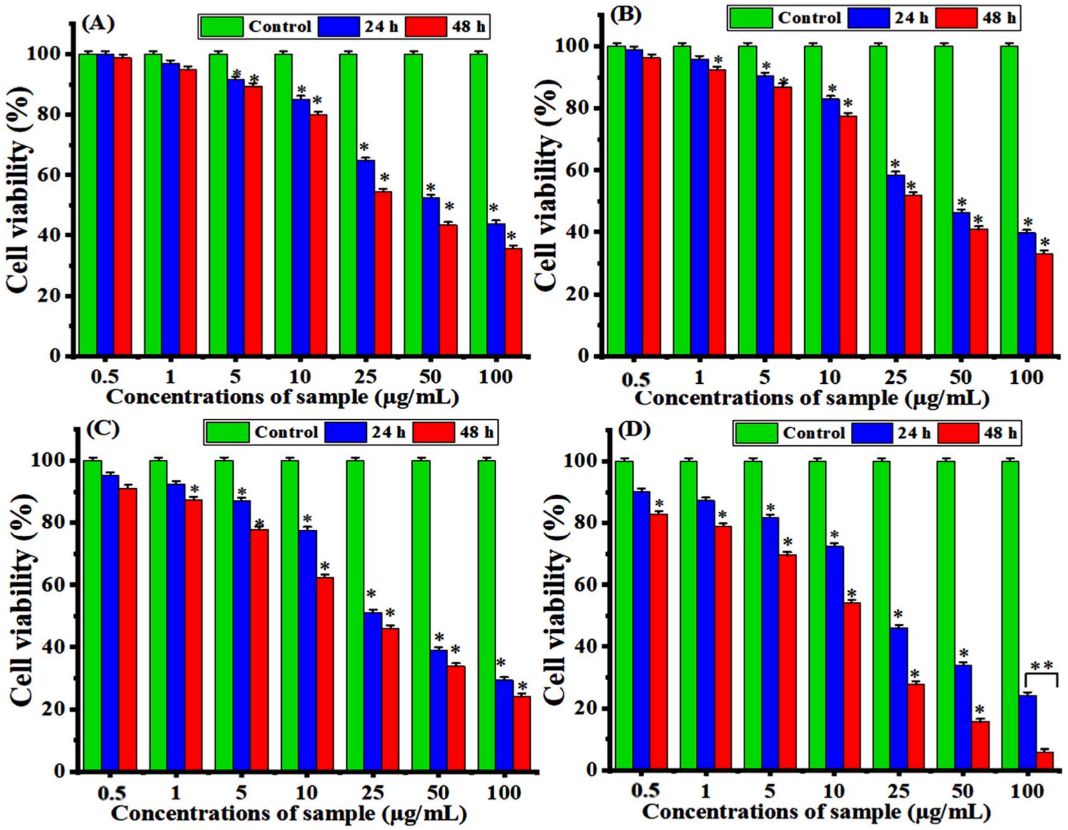

Fig. 10 Cytotoxicity of the synthesized samples toward the breast (MCF-7) cancer cells for 24 h and 48 h using MTT assay: (A) pure TiO_2 NPs, (B) ZrO_2/TiO_2 NCs, (C) $CuO/ZrO_2/TiO_2$ NCs, and (D) $CuO/ZrO_2/TiO_2$/RGO NCs. Stars (*) indicate significant differences ($p < 0.05$) between the treated cells and controls.

impact their interaction with cell membranes through electrostatic repulsion. DLS results suggest that $CuO/ZrO_2/TiO_2$/RGO NC could be applied in potential medical applications.

3.9 Cytotoxicity and biocompatibility evaluations

Certain nanocomposites (NCs) have attractive potential application in medicine such as cancer therapy, biosensor, and drug delivery, as reported in previous studies.[85,86] Fig. 10A–D shows the anticancer results of the prepared samples for an exposure time of 24 h and 48 h toward MCF-7 cancer cells. It can be observed in Fig. 10A that the TiO_2 NPs exhibited moderate cytotoxicity against MCF-7 cells, with the cell viability decreasing as the concentration increased after 24 h. Under the same experimental conditions, after 48 hours, the cytotoxicity of these NPs was higher than that after 24 h through oxidative stress. These results were similar and supported with previous results.[87,88] Fig. 10B demonstrated that the ZrO_2/TiO_2 NCs show improved cytotoxicity compared to pure TiO_2 NPs, with a significant reduction in the cell viability after both 24 h and 48 h due to its stability. Similarly, $CuO/ZrO_2/TiO_2$ NCs (Fig. 10C) exhibited the highest cytotoxicity compared to TiO_2 and ZrO_2/TiO_2 NCs at lower concentrations. At higher concentrations, $CuO/ZrO_2/TiO_2$/RGO NCs (Fig. 10C) induced higher cytotoxicity compared to $CuO/ZrO_2/TiO_2$ NCs owing to the ability of the RGO sheet to improve the distribution of NCs and reduce their aggregation. We observed that the CuO, ZrO_2, and RGO sheets improved the

Table 2 IC_{50} values of the prepared samples for MCF-7 cells and HUVEC normal cells

	MCF-7 cell lines		HUVEC normal cells	
	IC_{50} (μg mL^{-1} ± SD)		IC_{50} (μg mL^{-1} ± SD)	
Prepared samples	24 h	48 h	24 h	48 h
Pure TiO_2 NPs	73.98 ± 0.9	50.64 ± 1.1	1613.11 ± 10.1	1201.20 ± 9.6
ZrO_2/TiO_2 NCs	53.17 ± 0.7	43.39 ± 1.3	1021 ± 5.4	1836.03 ± 7.8
$CuO/ZrO_2/TiO_2$ NC	47.41 ± 1.0	34.03 ± 1.5	9251 ± 4.9	850.398 ± 6.2
$CuO/ZrO_2/TiO_2$/RGO NCs	44.19 ± 1.2	24.52 ± 0.8	1923.21 ± 9.3	723.07 ± 5.1

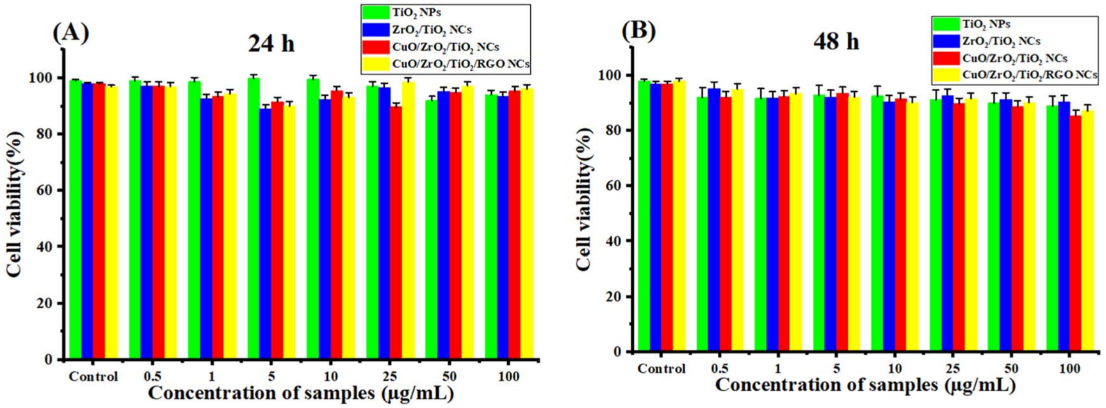

Fig. 11 Biocompatibilities of the synthesized TiO_2 NPs, ZrO_2/TiO_2 NCs, $CuO/ZrO_2/TiO_2$ NCs, and $CuO/ZrO_2/TiO_2$/RGO NCs toward the HUVEC normal cells using MTT assay: (A) 24 h and (B) 48 h.

cytotoxicity compared with each prepared sample. Table 2 shows the half maximal inhibitory concentration (IC_{50}) values. These values exhibited that $CuO/ZrO_2/TiO_2$/RGO NCs have the highest cytotoxicity activity toward MCF-7 cells, with the lowest IC_{50} value (24.52 µg mL^{-1}) at 48 h. These results suggest a synergistic effect from the structure of the prepared NPs and NCs and improved cell uptake. Additionally, this study highlighted that the combined $CuO/ZrO_2/TiO_2$ NC with RGO could hold potential as an anticancer agent due to the increased damage to cancer cells. Additionally, all samples show greater cytotoxicity with longer exposure, as seen from the lower IC_{50} values at 48 h compared to those at 24 h. In this study, we did not study the possible mechanisms of selective cytotoxicity of the present nanocomposites. However, earlier studies suggest that such types of nanocomposites exhibit anticancer activity through induction of oxidative stress.[89,90] The outcome of this work paves the way for future research to delineate the plausible mechanisms of anticancer potential of $CuO/ZrO_2/TiO_2$/RGO NCs.

The cell viability of HUVEC normal cells after two exposure times of 24 h and 48 h at concentrations (0.5, 1, 5, 10, 25, 50 and 100 µg mL^{-1}) was measured, as presented in Fig. 11A and B. They observed that the cell viability remains nearby 100–85% for all the concentrations. This result indicates that the synthesized NPs and NCs are highly biocompatible with HUVEC cells. However, these samples are slightly cytotoxic at a high concentration of 100 µg mL^{-1} for 48 h (Fig. 11B) against HUVEC normal cells since the cell viability does not drop near or below 50%. In the present work, the IC_{50} of HUVEC normal cells is not feasible within the selected concentrations, as shown in Table 2. This result shows that these samples likely have an IC_{50} much higher than 100 µg mL^{-1} for HUVEC cells, which supports their biocompatibility.

4. Conclusion

In summary, the chemical co-precipitation process was successfully applied to fabricate $CuO/ZrO_2/TiO_2$/RGO NCs to improve their selective anticancer activity. XRD, HRTEM, SEM, XPS, Raman, FTIR, PL, and DLS were carefully used to examine the properties of the produced samples. XRD data showed that the supporting CuO, ZrO_2, and RGO sheets for pure TiO_2 NPs impact their phase and crystalline size. Surface spherical morphology and increased particle size of the prepared samples were confirmed through TEM and HRTM images. The percentage of elemental compositions (Cu, Zr, Ti, O, and C) and their distribution in the fabricated $CuO/ZrO_2/TiO_2$/RGO NCs were determined from EDX analysis. XPS results showed the chemical compositions and chemical state of the prepared NCs. Raman and FTIR spectra determined the functional groups and crystal structure. PL analysis revealed that the reduction of PL intensities of the obtained samples was due to reduced electron–hole recombination rates. DLS demonstrated that the colloidal stability and distribution of $CuO/ZrO_2/TiO_2$/RGO NC were greater than those of the individual samples in the suspension of the media culture. It can be exhibited that the negative charges on the surface of NPs and NCs could impact their interaction with cell membranes through electrostatic repulsion. *In vitro* study showed that the $CuO/ZrO_2/TiO_2$/RGO NCs have the highest anticancer activity (cytotoxicity) against breast cancer (MCF-7) cells compared to individual samples at high concentrations for 48 h. For the biocompatibility test, this result indicates that the synthesized NPs and NCs are highly biocompatible with HUVEC cells. Additionally, IC_{50} values of $CuO/ZrO_2/TiO_2$/RGO NCs (44.19 ± 1.2 µg mL^{-1} and 24.52 ± 0.8 µg mL^{-1} for 24 h and 48 h) were greater than those of each of the prepared samples. These results highlight that $CuO/ZrO_2/TiO_2$/RGO NCs have the ability to kill cancer cells for the enhanced anticancer performance of TiO_2 NPs. This study should investigate their therapeutic performance on various cancer cell lines and *in vivo* model.

Data availability

The data supporting this work can be obtained from the corresponding author upon request.

Author contributions

Z. M. A. conceptualized the study, and the investigations and methods were carried out by Z. M. A., H. A. A., M. A. and S. A.

The original draft was prepared by Z. M. A. Review and editing were conducted by Z. M. A., H. A. A., M. A. and S. A. All the authors reviewed and approved the final version of the text for publication.

Conflicts of interest

This work is original research and has not been submitted for publication elsewhere.

Acknowledgements

The authors extend their sincere appreciation to researchers supporting project number (RSPD2024R813), King Saud University, Riyadh, Saudi Arabia for funding this research.

References

1 S. Quader and K. Kataoka, *Mol. Ther.*, 2017, **25**(7), 1501–1513.
2 Q. Zhou, L. Zhang and H. Wu, *Nanotechnol. Rev.*, 2017, **6**, 473–496.
3 Z. Jing, Q. Du, X. Zhang and Y. Zhang, *Chem. Eng. J.*, 2022, **446**, 137–147.
4 J. Jeevanandam, J. K. U. Ling, A. Barhoum, Y. S. Chan and M. K. Danquah, *Fundamentals of Bionanomaterials*, 2022, pp. 1–29.
5 Z. Yin, L. Wu, H. G. Yang and Y. Su, *Phys. Chem. Chem. Phys.*, 2013, **15**(14), 4844–4858.
6 A. Mansoor, Z. Khurshid, M. T. Khan, E. Mansoor, F. B. Butt, A. Jamal and P. J. Palma, *Nanomaterials*, 2022, **12**, 3670.
7 S. Sargazi, S. Er, S. S. Gelen, A. Rahdar, M. Bilal, R. Arshad, N. Ajalli, M. F. A. Khan and S. Pandey, *J. Drug Delivery Sci. Technol.*, 2022, **75**, 103605.
8 Z. E. Allouni, M. R. Cimpan, P. J. Høl, T. Skodvin and N. R. Gjerdet, *Colloids Surf., B*, 2009, **68**(1), 83–87.
9 A. Y. Elderdery, B. Alzahrani, A. Alabdulsalam, S. M. A. Hamza, A. M. E. Elkhalifa, A. H. Alhamidi, F. Alanazi, A. Mohamedain, S. K. Subbiah and P. L. Mok, *Bioinorg. Chem. Appl.*, 2022, **1**, 6835625.
10 S. f. Alanazi, Z. M. Alaizeri, R. Lateef, N. Madkhali, A. Alharbi and M. Ahamed, *Appl. Sci.*, 2023, **13**, 12456.
11 P. Sivakumar, M. Lee, Y.-S. Kim and M. S. Shim, *J. Mater. Chem. B*, 2018, **6**(30), 4852–4871.
12 Y. T. Gebreslassie and F. G. Gebremeskel, *Biotechnol. Rep.*, 2024, **44**, e00828.
13 Y. Shang, Q. Wang, J. Li, H. Liu, Q. Zhao, X. Huang, H. Dong, W. Chen, R. Gui and X. Nie, *Front. Chem.*, 2021, **9**, 522708.
14 A. J. Talaei, N. Zarei, A. Hasan, S. H. Bloukh, Z. Edis, N. A. Gamasaee, M. Heidarzadeh, M. M. N. Babadaei, K. Shahpas and, M. Sharifi, K. Akhatri, S. Khan, M. Xue and M. Falahati, *Arabian J. Chem.*, 2021, **14**, 102923.
15 A. T. Mohamed, R. A. Hameed, S. H. EL-Moslamy, M. Fareid, M. Othman, S. A. Loutfy, E. A. Kamoun and M. S. Elnouby, *Sci. Rep.*, 2024, **14**, 6081.
16 Z. Lin, N. Goswami, T. Xue, O. J. H. Chai, H. Xu, Y. Liu, Y. Su and J. Xie, *Adv. Funct. Mater.*, 2021, **31**, 2105662.
17 X. Liu, J. Iocozzia, Y. Wang, X. Cui, Y. Chen, S. Zhao, Z. Li and Z. Lin, *Energy Environ. Sci.*, 2017, **10**, 402–434.
18 D. Y. Nadargi, M. S. Tamboli, S. S. Patil, R. B. Dateer, I. Mulla, H. Choi and S. S. Suryavanshi, *ACS Omega*, 2020, **5**, 8587–8595.
19 P. Sable, N. Thabet, J. Yaseen and G. Dharne, *Trends Sci.*, 2022, **19**, 3092.
20 S. C. Yadav, N. Rani and K. Saini, *IOP Conf. Ser.:Mater. Sci. Eng.*, 2022, 012004.
21 A. Kubiak, K. Siwińska-Ciesielczyk and T. Jesionowski, *Materials*, 2018, **11**, 2295.
22 V. Isahi, C. Maghanga, M. Mwamburi, O. Munyati, S. Hatwaambo, E. Akoto, W. Isoe and M. W. Alam, *Tanzan. J. Sci.*, 2023, **49**, 590–602.
23 D. Paul, S. Mangla and S. Neogi, *Mater. Lett.*, 2020, **271**, 127740.
24 M. A. Marsooli, M. Fasihi-Ramandi, K. Adib, S. Pourmasoud, F. Ahmadi, M. R. Ganjali, A. S. Nasab, M. R. Nasrabadi and M. E. Plonska-Brzezinska, *Materials*, 2019, **12**, 3274.
25 T. Indumathi, J. Suriyaprakash, A. A. Alarfaj, A. H. Hirad, R. Jaganathan and M. Mathanmohun, *J. Basic Microbiol.*, 2024, **64**, 2300505.
26 N. Thiyagarajulu, P. Deepak, C. Kamaraj, K. A. Al-Ghanim, A. Lakshminarayanan, M. Nicoletti, S. Arumugam and M. Govindarajan, *Biomass Convers. Biorefin.*, 2023, 1–15.
27 N. K. Kadiyala, B. K. Mandal, L. V. K. Reddy, C. H. W. Barnes, L. D. L. S. Valladares and D. Sen, *ACS Omega*, 2023, **8**, 2406–2420.
28 M. Ahamed, M. J. Akhtar and M. Khan, *Mater. Today Commun.*, 2023, **36**, 106756.
29 L. Scotti, A. Aceto, B. B. Manshian, M. Ahamed, R. Lateef, M. A. M. Khan, P. Rajanahalli and M. J. Akhtar, *J. Funct. Biomater.*, 2023, **14**, 1–38.
30 Z. M. Alaizeri, H. A. Alhadlaq, S. Aldawood, M. J. Akhtar and M. Ahamed, *ACS Omega*, 2023, **8**, 25020–25033.
31 Z. M. Alaizeri, H. A. Alhadlaq, S. Aldawood and N. A. Y. Abduh, *RSC Adv.*, 2024, **14**, 16685–16695.
32 N. Askari, M. Askari and A. Di Bartolomeo, *J. Electrochem. Soc.*, 2022, **169**, 106511.
33 N. Askari, M. Askari and A. Di Bartolomeo, *J. Electrochem. Soc.*, 2022, **169**, 106511.
34 Z. A. M. Alaizeri, H. A. Alhadlaq, S. Aldawood and N. A. Y. Abduh, *RSC Adv.*, 2024, **14**, 16685–16695.
35 Z. M. Alaizeri, H. A. Alhadlaq, S. Aldawood, M. J. Akhtar and M. Ahamed, *ACS Omega*, 2023, **8**, 25020–25033.
36 Z. A. M. Alaizeri, H. A. Alhadlaq, S. Aldawood, M. J. Akhtar and M. Ahamed, *Environ. Sci. Pollut. Res.*, 2023, **30**, 6055–6067.
37 Z. M. Alaizeri, H. A. Alhadlaq, S. Aldawood, J. Akhtar and M. Ahamed, *Polymers*, 2022, **14**, 2036.
38 E. Abdolmajid, H. Kharazi, M. M. Chalaki, M. Khojasteh, S. Haghighat, F. Attar, F. Nemati and M. Falahati, *J. Biomol. Struct. Dyn.*, 2018, **37**, 3007–3017.
39 M. Baithy, D. Mukherjee, A. Rangaswamy and B. M. Reddy, *Catal. Lett.*, 2022, **152**, 1428–1440.
40 M. Kikugawa, K. Yamazaki and H. Shinjoh, *Appl. Catal., A*, 2017, **547**, 199–204.

41 M. T. Ulhakim, S. Sukarman, K. Khoirudin, N. Fazrin, T. Irfani and A. Hakim, *Indones. J. Appl. Phys.*, 2024, **14**, 141–150.
42 H. Koohestani and S. K. Sadrnezhaad, *Desalin. Water Treat.*, 2016, **57**, 28450.
43 T. H. Nguyen, T. L. Nguyen, T. D. T. Ung and Q. L. Nguyen, *Adv. Nat. Sci.:Nanosci. Nanotechnol.*, 2013, **4**, 025002.
44 R. R. Muthuchudarkodi and C. Vedhi, *Adv. Mater. Res.*, 2013, **678**, 50–55.
45 N. Yaacob, A. F. Ismail, G. P. Sean and N. A. M. Nazri, *SN Appl. Sci.*, 2019, **1**, 1–14.
46 S. Bhattacharjya, T. Adhikari, A. Sahu and A. K. Patra, *Ecotoxicology*, 2021, **30**, 719–732.
47 A. Fall, I. Ngom, M. Bakayoko, N. F. Sylla, H. E. A. Mohamed, K. Jadvi, K. Kaviyarasu and B. D. Ngom, *Mater. Today: Proc.*, 2021, **36**, 349–356.
48 D. Guerrero-Areque, R. Gómez and H. A. Calderon, *Microsc. Microanal.*, 2017, **23**, 2036–2037.
49 D. Guerrero-Areque, R. Gómez and H. A. Calderon, *Microsc. Microanal.*, 2017, **23**, 2036–2037.
50 Y. N. Sudhakar, H. Hemant, S. Nitinkumar, P. Poornesh and M. Selvakumar, *Ionics*, 2017, **23**, 1267–1276.
51 M. R. Shaik, M. Alam, S. F. Adil, M. Kuniyil, A. A. Al-Warthan, M. R. H. Siddiqui, M. N. Tahir, J. P. Labis and M. Khan, *Materials*, 2019, **12**, 711.
52 K. V. Bineesh, D.-K. Kim and D.-W. Park, *Nanoscale*, 2010, **2**(7), 1222–1228.
53 J. Tasiu, M. Y. Onimisi, A. S. Yusuf, E. Danladi and N. N. Tasie, *East Eur. J. Phys.*, 2024, **1**, 315–321.
54 L. J. Tomar and B. S. Chakrabarty, *Adv. Mater. Lett.*, 2013, **4**, 64–67.
55 R. R. Muthuchudarkodi and C. Vedhi, *Adv. Mater. Res.*, 2013, **678**, 50–55.
56 L. Jayasinghe, V. Jayaweera, N. de Silva and A. M. Mubarak, *Mater. Adv.*, 2022, **3**, 7904–7917.
57 A. G. Bekru, L. T. Tufa, O. A. Zelekew, J. Gwak, J. Lee and F. K. Sabir, *Crystals*, 2023, **13**, 133.
58 I. M. Sharaf, J. Laifi, S. W. Alraddadi, M. Saad, M. S. I. Koubesy, N. N. Elewa, H. Almohiy, Y. A. M. Ismail, A. Soldatov and A. M. Aboraia, *Heliyon*, 2024, **10**, 1.
59 A. Thakur, S. Kumar, G. Singh and V. S. Rangra, *Mater. Today: Proc.*, 2022, **9**, 129.
60 S. G. Babu, R. Vinoth, D. Praveen Kumar, M. V. Shankar, H. L. Chou, K. Vinodgopal and B. Neppolian, *Nanoscale*, 2015, **7**, 7849–7857.
61 D. Cosma, A. Urda, T. Radu, M.-C. Roşu, M. Miheţ and C. Socaci, *Molecules*, 2022, **27**, 5803.
62 L. Martin, H. Martínez, D. Poinot, B. Pecquenard and F. Le Cras, *J. Phys. Chem. C*, 2013, **117**, 4421–4430.
63 M. C. Biesinger, *Surf. Interface Anal.*, 2017, **49**, 1325–1334.
64 J. Qian, Q. Hu, X. Hou, F. Qian, L. Dong and B. Li, *Ind. Eng. Chem. Res.*, 2018, **57**(38), 12792–12800.
65 K. V. R. Chary, G. V. Sagar, D. Naresh, K. K. Seela and B. Sridhar, *J. Phys. Chem. B*, 2005, **109**(19), 9437–9444.
66 Q. T. Trinh, K. Bhola, P. N. Amaniampong, F. Jérôme and S. H. Mushrif, *J. Phys. Chem. C*, 2018, **122**(39), 22397–22406.
67 K. Dong, J. He, J. Liu, F. Li, L. Yu, Y. Zhang, X. Y. Zhou and H. Ma, *J. Mater. Sci.*, 2017, **52**, 6754–6766.
68 N. J. Ananth, R. G. S. Rao, V. S. Vinita, J. Samuel, S. Shabna, P. M. S. Shinu, S. Suresh, Y. Samson and C. S. Biju, *Phosphorus, Sulfur Silicon Relat. Elem.*, 2021, **197**, 164–168.
69 M. Baithy, D. Mukherjee, A. Rangaswamy and B. M. Reddy, *Catal. Lett.*, 2022, **152**, 1428–1440.
70 Ma. Manríquez, M. Picquart, X. Bokhimi, T. López, P. Quintana and J. M. Coronado, *J. Nanosci. Nanotechnol.*, 2008, **8**(12), 6623–6629.
71 M. Z. U. Shah, M. Sajjad, H. Hou, S. ur Rahman, A. Mahmood, U. Aziz and A. Shah, *J. Energy Storage*, 2022, **55**, 105492.
72 E. Hajialilou, H. Asgharzadeh and S. Khameneh Asl, *Appl. Surf. Sci.*, 2021, **544**, 148832.
73 S. Sagadevan, J. Podder and I. Das, *J. Mater. Sci.: Mater. Electron.*, 2016, **27**, 5622–5627.
74 M. Ikram, J. Hassan, A. Raza, A. Haider, S. Naz, A. Ul-Hamid, J. Haider, I. Shahzadi, U. Qamar and S. Ali, *RSC Adv.*, 2020, **10**, 30007–30024.
75 M. Chen, T. P. Straatsma and D. A. Dixon, *J. Phys. Chem. A*, 2015, **119**(46), 11406–11421.
76 A. K. Singh and U. T. Nakate, *Sci. World J.*, 2014, **1**, 349457.
77 L. Li, X. Qu, G. Pan and J. H. Jeong, *Chemosensors*, 2024, **12**, 62.
78 D. Bala, I. Matei, G. Ioniţă, D. Cosma, M.-C. Roşu, M. Stanca, C. Gaidău, M. Baleanu, M. Virgolici and I. R. Stanculescu, *Int. J. Mol. Sci.*, 2022, **23**, 14703.
79 E. Hajialilou, H. Asgharzadeh and S. Khameneh Asl, *Appl. Surf. Sci.*, 2021, **544**, 148832.
80 N. Subha, M. Mahalakshmi, M. Myilsamy, N. Lakshmana Reddy, M. V Shankar, B. Neppolian and V. Murugesan, *Int. J. Hydrogen Energy*, 2018, **43**, 3905–3919.
81 S. Saukani, *UIN Sunan Gunung Djati Bandung*, 2018.
82 Y. V Larichev, *Inorganics*, 2022, **10**, 248.
83 J. M. Berg, A. A. Romoser, N. Banerjee, R. Zebda and C. M. Sayes, *Nanotoxicology*, 2009, **3**, 276–283.
84 A. H. Shah and M. A. Rather, *Mater. Today: Proc.*, 2021, **44**, 482–488.
85 A. K. Nayak, S. Alkahtani and M. Saquib Hasnain, *Biomed. Compos.*, 2021, 35–69.
86 S. U. R. Qamar, *Colloid Interface Sci. Commun.*, 2021, **43**, 100463.
87 M. J. Basante-Romo, Ó. Gutiérrez and R. J. Camargo-Amado, *Inf. Tecnol.*, 2016, **27**, 63–68.
88 R. Vigneshwaran, D. Ezhilarasan and S. Rajeshkumar, *Inorg. Chem. Commun.*, 2021, **133**, 108920.
89 M. Ahamed, M. J. Akhtar, M. A. M. Khan and H. A. Alhadlaq, *Int. J. Nanomed.*, 2021, **16**, 89–104.
90 C. S. Chakra, V. Rajendar, K. V. Rao and M. Kumar, *3 Biotech*, 2017, **7**, 1–8.